Chapter 4
Microstructure Development: Solidification and Isothermal Aging

The formation of a solder joint is described from initial solidification to aging effects. In the Sn–Ag–Cu alloy system, joints tend to form as either single crystals or tri-crystals that have twin interfaces that form a "beachball" orientation relationship of 60° sections about a common [100] axis. The effect of the anisotropic coefficient of thermal expansion and elastic modulus on microstructure development and initial states of internal stress as the joint solidifies and cools is examined. Due to this anisotropy, the grain orientations and the position of the joint in the package and the stress state and its evolution are unique for each joint. The local properties and microstructure of the joint are sensitive to minor alloying additions that can be introduced via the metallization layers on both the circuit board and the package. With isothermal aging, complexities arising from microalloying elements can be either beneficial or detrimental, and these issues are illustrated following Ni, P, and Pd microalloying elements to show that microalloying can be strategically used to manage and design both the solder and the interfacial properties.

The Beginning: The Initial Microstructure

Chapter three identified how sensitive solidification microstructures are to alloy composition and cooling rate, noting especially how forming a β-Sn nucleus often requires substantial undercooling. Additional complications arise from dissolution of interfacial metals into the melt, which introduce concentration gradients into the liquid solder. The composition of the liquid will depend on all that happens in the liquid during the minute or so of the reflow event. Because solder joints solidify in a nonequilibrium manner, the solidification process depends strongly on the concentration and temperature gradients just before solidification commences. The free surfaces associated with the shape of the joint provide an additional boundary condition that affects solidification of the joint. In addition, if there are large intermetallic phases present in the solder, it takes time for them to dissolve. If the IMC

© Springer Science+Business Media New York 2015

T.-K. Lee et al., *Fundamentals of Lead-Free Solder Interconnect Technology*,
DOI 10.1007/978-1-4614-9266-5_4

phases are not dissolved before solidification commences or if they form in the liquid before the tin starts to solidify, they can affect the solidification process and hence, the microstructure that develops. As long as there are no unmelted phases in the liquid solder prior to solidification in the reflow event, then any prior history before melting has minimal importance on the future microstructural evolution of the joint.

Given that the reflow process has a strong influence on the solidification process (especially the concentration and thermal gradients present in the liquid) [1–4], this will be the starting point for describing the evolution of the microstructure of a solder joint. In this chapter, the conditions that affect formation of the initial solidification microstructure will be the primary focus. As the solidification microstructure forms in a highly nonequilibrium manner, driving forces for continued changes remain in the microstructure. However, if the joint does not melt completely, the implications of this, as well as the potential for fabricating joints without complete melting (i.e., semisolid joint formation), will be discussed first.

Solid-State and Semisolid Joint Formation

While Sn-based solders are heavily used, there is a growing need for higher-temperature interconnection materials. One approach in making higher-temperature joints is to use solid-state diffusional (sintering) processes. An important area of current research involves the use of nanoscale particles to form a joint capable of high-temperature performance [5–7]. The nanoscale particle size has a high surface-to-volume energy ratio, and this surface energy is a form of stored free energy that can cause incipient melting far below the normal melting temperature. The surface energy is high enough to enable rapid sintering of nanoscale powders to form a structural joint once the temperature is high enough to initiate incipient melting, where the liquid greatly accelerates the sintering process. Once this starts, the transport distances are nanoscale in the interfacial liquid, so the formation of a nearly fully dense joint can happen in a short time at a temperature more than 100 °C below the equilibrium melting temperature. A major challenge with this approach is to keep the nanoscale powder from becoming oxidized prior to the sintering operation and to insure that protective coatings are removed. Subsequent remelting of joints made in this manner require heating to the normal melting temperature because the surface energy present in the nanoscale powder was used and dissipated to form the joint and is no longer available to lower the thermal energy needed to melt.

The approach just described is similar to a more general approach called transient liquid phase bonding or solid–liquid interdiffusion (TLPB, SLID) [8, 9]. This semisolid approach involves making a paste of powders that can form a low melting temperature eutectic composition at the interfaces (even though the overall composition can be far from the eutectic composition). Once the eutectic temperature is reached, the interfacial regions on the powder particle surfaces melt, and the liquid then spreads into the interfacial regions, partially dissolving the solids on either side

of the liquid. It is not necessary to fully melt the two phases in the powder, as long as there is enough liquid formed to facilitate mass transport to eliminate most of the porosity. When this process is well designed it is possible to have less shrinkage porosity than normal melting, because only a fraction of the material goes through the liquid to solid phase transformation [10]. It is important to decide whether a homogeneous composition is needed, as composition gradients generate a chemical potential that can affect further evolution of the microstructure in desirable (e.g., composition homogenization) or undesirable ways (e.g., galvanic potential that enhances corrosion).

Yet another approach to making a high-temperature interconnect is to start with a low melting temperature solder joint using a Sn-based solder to connect two copper substrates. With time and temperature, the Sn will be slowly consumed to make Cu_6Sn_5 and Cu_3Sn intermetallic phases. These two intermetallic phases have a much higher melting temperature than Sn, but they are not very ductile. This approach is most useful if the two copper pieces to be joined are not needed to mitigate differential thermal expansion requirements, so this strategy can be considered for joining components with the same expansion properties. However, if differential expansion needs to be accommodated, maintaining a softer solder joint may be necessary to prevent cracking of the joint or the components to be joined. Issues regarding consumption of Sn to form intermetallics, and thermal fatigue of Sn-based joints in settings where Sn is consumed by Cu will be discussed further in later sections.

Intrinsic Anisotropy of Sn

One of the most important fundamental issues with Sn-based solders was hidden from view in Sn–Pb alloys; Sn is one of the most anisotropic metals in the periodic table. The crystal structure of Sn is illustrated in Fig. 4.1, where its body-centered tetragonal structure shows a central atom with tetrahedral bonding to the atoms on

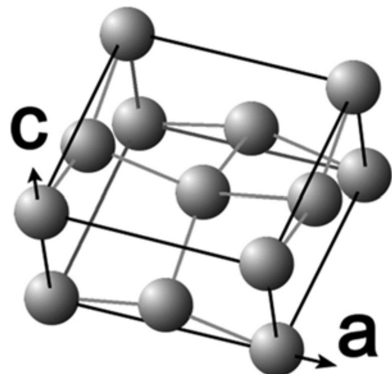

Fig. 4.1 Crystal structure of pure Sn (A5, tI4, space group 141, I41/amd) with lattice parameters a =5.8315 Å, c =3.1814 Å; c/a=0.5456

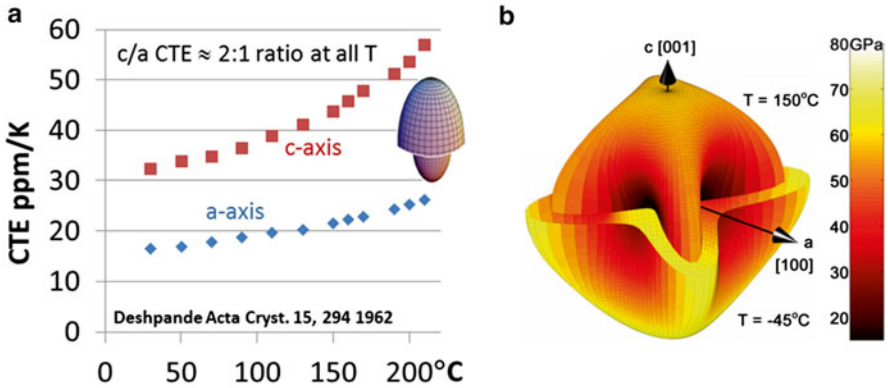

Fig. 4.2 (**a**) Temperature dependence of the coefficient of thermal expansion (CTE) with temperature in the directions the half- (*ellipses* show relative difference in CTE magnitude at 25 and 210 °C). (**b**) Anisotropy of Young's Modulus at −40 and 150 °C

the four faces. The Sn structure is essentially a squashed diamond cubic structure.[1] When Sn is combined with Pb, which is much softer than Sn and has more isotropic plastic properties, the Pb accommodates the anisotropic deformation of Sn. As Sn-based joints often form large or single-crystal joints, the anisotropic properties of Sn provide an important driving force for heterogeneous microstructural evolution, and hence the properties of solder joints evolve in a complex manner. Figure 4.2 and Table 4.1 illustrate and summarize the physical properties of Sn [11–13]. Of particular importance is the anisotropy of the coefficient of thermal expansion (CTE) plotted in Fig. 4.2a. The CTE increases with a slight upward curvature with temperature, and it is twice as large in the *c* direction than the *a* direction, at all temperatures. The 3-dimensional CTE surface that describes this property with respect to the crystal directions has the appearance of an ellipsoid. Hence, the CTE is isotropic in the x–y plane and shows the maximum anisotropy in any plane containing the z axis.

The elastic anisotropy is greater than the CTE anisotropy and is illustrated as a surface of Young's modulus values in 3 dimensions in Fig. 4.2b. This figure is shown at two temperatures, the upper half at 150 °C and the lower half at −45 °C, which bounds the typical range of application temperatures for most electronic systems. Sn is most compliant in the <100] directions and stiffest in the [001] direction and almost as stiff in the <110] directions (hence, Sn is nearly isotropic on <110) planes). At low temperatures, the maximum anisotropy ratio is about 2, but this ratio increases to about 5 at the highest temperatures. An important non-intuitive outcome of the stiffness and CTE is that Sn is stiffest in the direction that the CTE is

[1] While there are only four atoms in the Sn unit cell and eight in the diamond cubic unit cell, the connectivity of the tetrahedral bonding arrangement is the same. More atoms are required in the diamond cubic unit cell to describe the symmetry than the tetragonal Sn unit cell.

Table 4.1 Important anisotropic physical properties of Sn

Property	Direction[a]			Reference
	<100]	<110]	[001]	
Young's Modulus at −45 °C	28.7	65.9	71.4	11, 12
Young's Modulus at 22.5 °C	23.5	62.4	66.6	11, 12
Young's Modulus at 150 °C	13.3	54.5	57.7	11, 12
CTE at 30 °C	16.5	16.5	32.4	13
CTE at 160 °C	22.3	22.3	45.9	13
Diffusivity[b] of Sn	10.7, 105.1	10.7, 105.1	7.7, 107.2	72
Diffusivity of Ag in Sn	0.018, 77.0	0.018, 77.0	7.1e-3, 51.5	73
Diffusivity of Cu in Sn	2.4e-3, 33.1	2.4e-3, 33.1	D = 2e-6	74
Diffusivity of Ni in Sn	1.87e-2, 54.2	1.87e-2, 54.2	1.92e-2, 18.1	75
Electrical resistivity	ρ_0	ρ_0	$1.48\rho_0$	76

[a]Use of mixed braces <*uvw*] and <*hkl*) represents the symmetry of the tetragonal crystal structure; the first two indices are permutable, to be in the same family. Crystal directions *[uvw]* and plane normal directions *(hkl)* in a crystal based Cartesian coordinate system are *[ua va wc] and (h/a k/a l/c)*
[b]Diffusivity values are D_o in cm^2/s and activation energy Q in kJ/mol

highest, and this implies that there will be profound disagreements at grain boundaries where dislocations are generated, leading to localized plastic deformation of the crystal. Hence, the amount of diffusion or dislocation generation required will be in proportion to the magnitude of the disorientation[2] between the two crystals and the change in stress or temperature.

Nonequilibrium Solidification

Solidification of alloys in practical time scales always involves nonequilibrium solidification processes that result in metastable microstructures, but the equilibrium phase diagram is useful to anticipate the direction of evolution of Sn–Ag and Sn–Cu phases as shown in Fig. 3.1. The Sn-rich corner of the ternary Sn–Ag–Cu phase diagram in Fig. 3.1b shows that the ternary eutectic temperature is lower than the eutectic temperatures of the binary alloys identified on the X and Y axes. As solder joints spend most of their lives above half their melting temperature (i.e. $0.5 \times (220+273)-273=-26.5$ °C), there is sufficient thermal energy for nonequilibrium microstructures to evolve into a state that is closer to equilibrium. Thus, understanding of solder joint property evolution depends on the starting nonequilibrium state of the solidification microstructure. Alloys such as SAC105 and SAC305 are

[2]The word misorientation is used loosely in the materials field and is often used to refer to "disorientation" too. Disorientation describes the angle of mismatch between two grains at a grain boundary. The word misorientation is used to refer to the difference in orientation between two locations within a grain and hence is descriptive of lattice curvature and low-angle boundaries.

hypoeutectic alloys, so primary solidification of Sn is expected to occur first (see table in Fig. 3.3). As the solidification of Sn commonly takes place at temperatures significantly lower than the eutectic temperature, the liquidus lines are projected below the eutectic temperature in Fig. 3.9. This implies that initial precipitation of Ag_3Sn or Cu_6Sn_5 could occur before Sn solidifies, even in a hypoeutectic alloy. An example of a nonequilibrium solidification path is illustrated for a Sn-3.8Ag-0.7Cu alloy in Fig. 3.9 and discussed in depth in the associated text. Solidification microstructures are greatly dependent on the solidification path that is actually followed, which depends on the details of nucleation of the Sn phase.

Typically, undercooling of 20–30 °C occurs in Sn-based solder joints. This is most commonly investigated using differential scanning calorimetry experiments. Figure 3.5 shows an example of a heating curve and Fig. 3.9 shows a cooling curve, where 15 °C undercooling is apparent before solidification started. Most other metals and alloys solidify with heterogeneous nucleation of the solid with only a few °C undercooling. At least two factors contribute to the need for much undercooling; firstly, the small volumes of solder joints reduce the probability of finding a critical nucleus. Secondly, the entropy of fusion of Sn is about 50 % larger than most other metals, implying that formation of a Sn unit cell/nucleus requires a larger amount of coordinated atomic positioning than other metals. The crystal structure[3] shown in Fig. 4.1 is body-centered tetragonal with 4 atoms per unit cell in a fairly open structure with tetrahedral bonding similar to diamond cubic (note the bonding arrangement of the central atom). The tetrahedral bonding (which may exist to some degree in the liquid) and the more open structure may account for a larger entropy change associated with crystallization than is found in other close-packed metals.

The larger entropy of fusion also leads to a larger-than-average release of heat with solidification, such that when solidification commences, recalescence can be significant. This effect is illustrated in the enthalpy diagram in Fig. 4.3a where the microstructure of a Sn–Ag solder ball shows a dendritic solidification microstructure. In the plot, an 80 °C undercooling condition is shown for illustrative convenience (which has occasionally been observed in isolated balls, but 30 °C is more typical), indicating that an 80 °C temperature increase is needed to bring the undercooled two phase solid + liquid into an equilibrium condition at the melting temperature. That is, the heat released by the enthalpy of fusion resulting from solidification reheats the sample to the melting temperature in a nearly adiabatic (constant enthalpy) process. Once the melting temperature is reached, a certain fraction of the Sn is solid, about 1/3 in the plot. It is likely that the fraction that solidifies adiabatically will occur quickly, and that once the two phase equilibrium temperature is reached, then the rest of the solder ball would solidify at the rate

[3] The density of α Sn in the diamond cubic structure is 5.769 g/cm^3 and β Sn in the body-centered tetragonal structure is 7.365 g/cm^3. If Sn atoms were in a face-centered cubic arrangement like Pb, then based upon the atom diameter defined by the closest spacing in the c direction, the density would be 8.75 g/cm^3, 19 % higher. Thus the BCT Sn crystal structure is more open than a close-packed lattice but denser than α Sn.

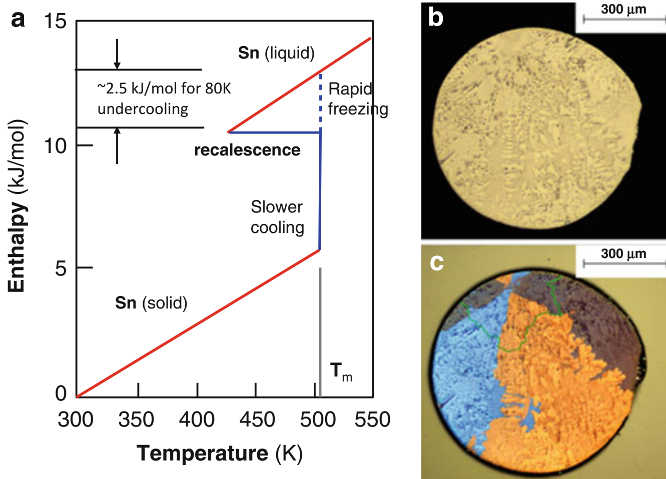

Fig. 4.3 (**a**) Enthalpy plot of Sn showing an exaggerated undercooling-recalescence path, and (**b**) a polished bright field optical image of a Sn-3.9Ag-0.6Cu solder ball polished through the center to illustrate a location close to the probable nucleation site. (**c**) Polarized light image of the same image showing a typically beachball microstructure, with an *overlaid line* illustrating a change in scale of solidification microstructure features that can be seen without distraction in (**b**)

imposed by the environment. Figure 4.3b, c illustrates a region near the pole that has much finer dendritic features than the rest of the solder ball. A green line in the polarized light image in (c) delineates the boundary between two scales of microstructural features [this boundary is easier to see in the bright field micrograph in (b)]. As finer microstructural features are a consequence of faster solidification rates, this boundary suggests that if solidification started at the pole of the beachball, a spherical cap with a diameter of about 1/2 of the diameter of the ball itself may have solidified much more quickly than the rest of the ball. This provides a way to correlate the recalescence event with the enthalpy plot. Using the formula for the volume of a spherical cap, this volume is about 4 % of the volume of the ball, which implies that this ball started to solidify after it undercooled at least 10 °C below the melting temperature (and hence, 4 % of the of the ball solidified adiabatically).

The solidification process has been monitored in situ in a synchrotron X-ray beam to identify some important features of the solidification process [14]. Figure 4.4 illustrates a sequence of 4 diffraction pattern images taken prior to melting, during the liquid state, at the moment of solidification and just after solidification, with integrated diffraction patterns overlaid. This solder joint was at the corner of a wafer-level chip-scale package (WLCSP) sample, so upon cooling, considerable strains developed as the sample cooled. Four important observations from these measurements are (1) the orientations of the crystal(s) before and after solidification are different (compare Fig. 4.4a, d), which implies that there is no obvious influence from the substrate on the orientation of the solidified joint; (2) the solidification took

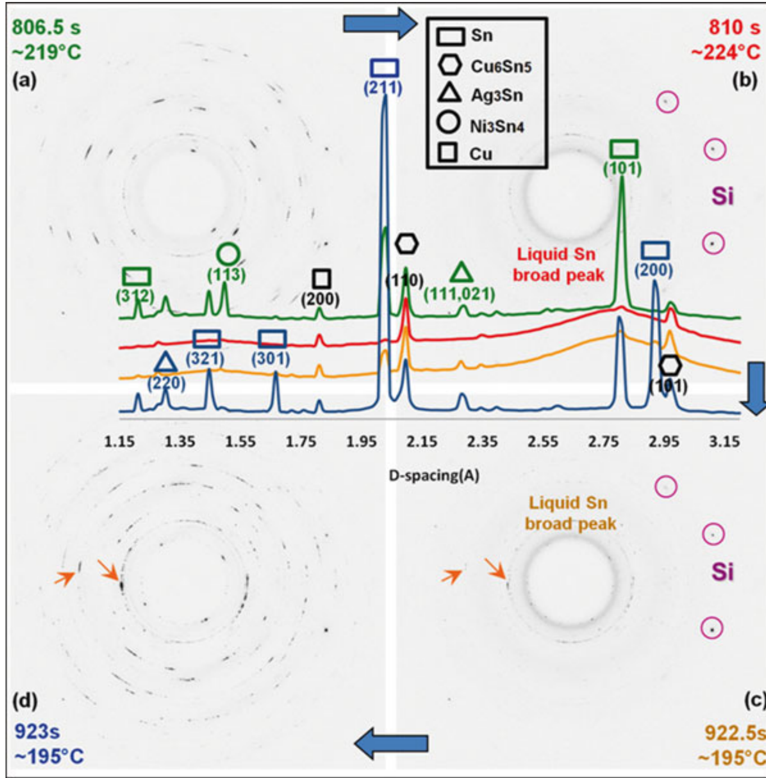

Fig. 4.4 In situ diffraction patterns during melting and solidification, illustrating how the Sn and Ag_3Sn peaks disappeared after melting and reappeared upon solidification. The *broad ring* indicates the liquid Sn phase. The Cu_6Sn_5 phase in the interface remained solid, as did Si (the Si chip was oriented to a nonsymmetric orientation in order to have few peaks). Solidification occurs within 1 s

place about 25 °C below the melting temperature; (3) the solidification process took place within 1 s, as images were taken at the rate of 2 per second; and (4) the orientations present just after solidification remained unaltered during the subsequent cooling process (not shown).

Figure 4.5 illustrates features of the beachball microstructure that are often seen in SAC solder joints, to compare different characterization methods and perspectives. In the top half of the figure, a series of polarized light images illustrate how the appearance is altered when the sample is oriented differently with respect to the polarized filters. Even a difference of 1.3° makes a noticeable change in the contrast of the different orientations, as the negatively sloped boundary is visible in the image marked 0° but only visible with knowledge that it is there in the image labeled −1.3°. The contrast reversed with a 90° rotation. This beachball structure has also been observed in other minerals such as aragonite and chrysoberyl and described as cyclic twins, owing to the repetition of interface disorientations about a common axis that

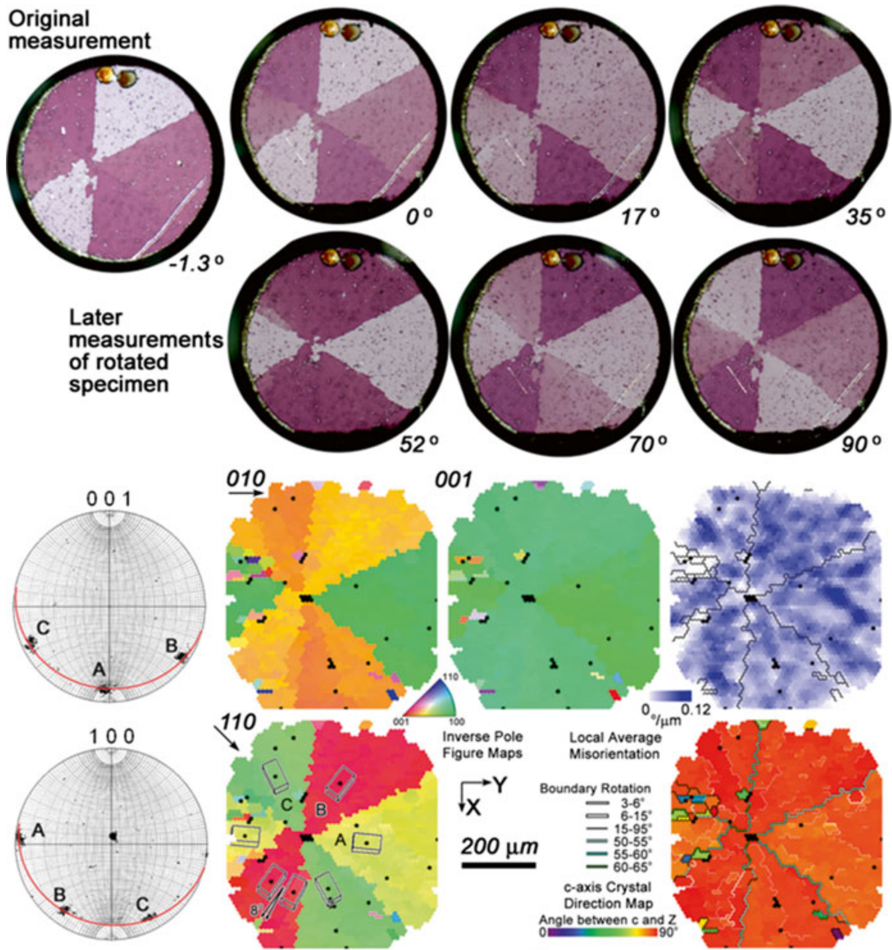

Fig. 4.5 The beachball microstructure of one particular SAC solder joint, showing three orientations arranged in six sections. It is characterized using several different polarized light filter orientations (the sample was rotated with a fixed filter condition, and then the images were rotated to have the ball in the same orientation on the page), and with different types of maps and pole figures made using an EBSP data set

sums to 360°. In the ideal beachball microstructure, there are six sections with three orientations, where the orientation on the opposite side has the same orientation and contrast, as illustrated in the figure. The beachball microstructure is more effectively characterized using scanning electron microscopy with electron backscattered diffraction pattern mapping (aka orientation imaging microscopy or OIM™), as illustrated in the lower part of Fig. 4.5. The left three maps are based upon inverse pole figure directions, where the color key is interpreted with respect to the sample [100], [001], and $[1\bar{1}0]$ directions, which give very different appearances. When the map

is referenced to the beachball axis direction (close to the [001] sample orientation), all sections have the same color, and hence the joint could appear as a single crystal. In order to clearly interpret the crystal orientations, at least two maps need to be made. The two orientation maps on the right illustrate other insightful ways to represent OIM data. Orientation gradient maps such as the local average misorientation show regions of greater and lesser lattice curvature, which varies spatially in every section, which will be discussed further below. Given the anisotropy related to the *c*-axis orientation, *c*-axis maps are often effective. In the lower right map, all three sections have a similar *c*-axis orientation with respect to the board, and hence, their color is similar, but minority orientations appear (small green grains) in a way that could be missed in other maps.

Depending on how the joint is cross-sectioned, the appearance of the beachball microstructure can vary significantly (sometimes hiding the threefold orientation relationship). In many cases, distortions in the shape of the three beachball orientations can be so strong, that only the pole figure will reveal that there are only three orientations having the beachball orientation relationship. Nevertheless, the orientation relationship between the three orientations exhibits a particular set of characteristics easily observed in pole figures.[4] The (001) and {100) pole figures in Fig. 4.5 illustrate the characteristic signature of a beachball orientation relationship. The three orientations present have a common [100] axis, which is near the center of the {100) pole figure for this ball (this common axis can have any orientation in a given joint). The other {100) poles show up three times for the other three orientations on a great circle 90° from the common (100) pole. The three (001) poles in the other pole figure are on the same great circle, at positions between the (010) poles.

A major concern about using 2-D sections is that nothing is known about the rest of the volume (though it can be inferred in many cases). Thus high-energy X-ray (synchrotron) measurements are useful because diffracted beams penetrate all the way through the sample. Figure 4.6 shows diffraction patterns for two balls out of a one row slice from a PBGA package [15]. Indexation of the pattern confirms that the full volume of many joints have one dominant orientation, and sometimes two orientations that are close to the same, indicating the presence of low-angle boundaries or a tri-crystal, as illustrated Fig. 4.7 shows a 14x14 plastic ball grid array in the as-solidified and aged state, sectioned parallel to the board interface. There are 38 joints (19 %) that are apparently single crystals this is an upper bound, see Fig. 4.5 which illustrates the limitations of this 2-dimensional cross-section method). This statistical analysis shows that SAC-type alloys tend to solidify as either single or tri-crystals [16–18].

---

[4] Pole figures show the orientation of crystal directions in the sample coordinate system. There is only one (001) pole in each crystal and two {100) poles, which are 90° apart, so that viewing the (001) pole figure allows the number of crystals to be identified, and with the {100) pole figure, one or a few orientations can be visualized.

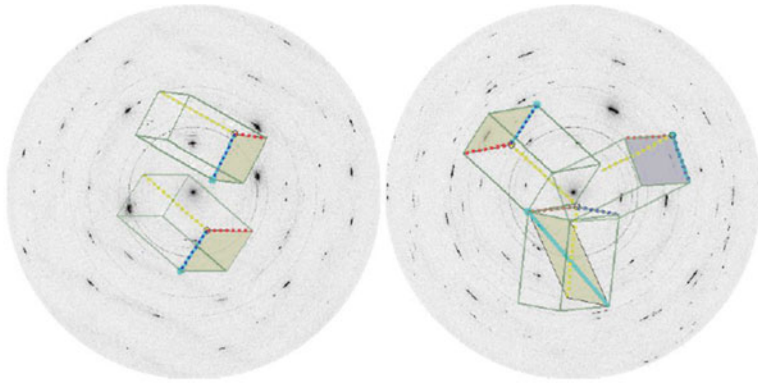

Fig. 4.6 Synchrotron diffraction pattern measurements of two different balls from a slice out of a package, illustrating one joint with two orientations that are close to each other, and another having a tri-crystal orientation relationship (slip planes with high Schmid factors in the vertical direction are illustrated)

Fig. 4.7 A 14×14 array of joints illustrating the variety of orientations of single and tri-crystal orientations. The *color code* is based upon the *c*-axis orientation with respect to the substrate. Ball D13 (4th row, 13th column) is examined in detail in Fig. 4.5

Sn Nucleation

From the discussion above, important factors that affect formation of a Sn nucleus were identified, so the actual nucleation process will be considered next. The fact that many joints solidify as single crystals implies that one nucleus forms and solidification takes place through the entire joint volume before another stable nucleus can form. Even if another stable nucleus does form in the joint prior to completion of solidification, the recalescence front at the solid–liquid interface is likely to remelt or destabilize it, such that the first growing nucleus will establish the orientation of the entire joint.

Given the strong driving force for rapid solidification arising from significant undercooling, the origin of the beachball orientation relationship described above must involve a nucleus that brings about all three orientations at the same time. Hence, a Sn-beachball nucleus requires formation of the nominally 60° interfaces at the time that a nucleus becomes stable. Recent investigations of this phenomenon in Sn have led to the hypothesis that a pseudo-hexagonal nucleus can form around an Ag atom at the center of a hexagonal unit cell, which enables growth to a size that is stable enough to then force three distinct Sn tetragonal orientations to develop radially [19]. Figure 4.8 shows how the {101)<101] twin system can form a 6-sided pseudo-hexagonal nucleus, such that Sn [100] directions radiate from the center, but this twin has a disorientation of 57.2°, not 60° [19]. Thus, misfit dislocations are required to compensate for the imperfect closure.

The fastest-growing crystal direction is <110], and these directions are illustrated on the related planar surfaces of the pseudohexagonal nucleus in Fig. 4.8 [20]. This shows that once this pseudohexagonal nucleus starts growing, the beachball

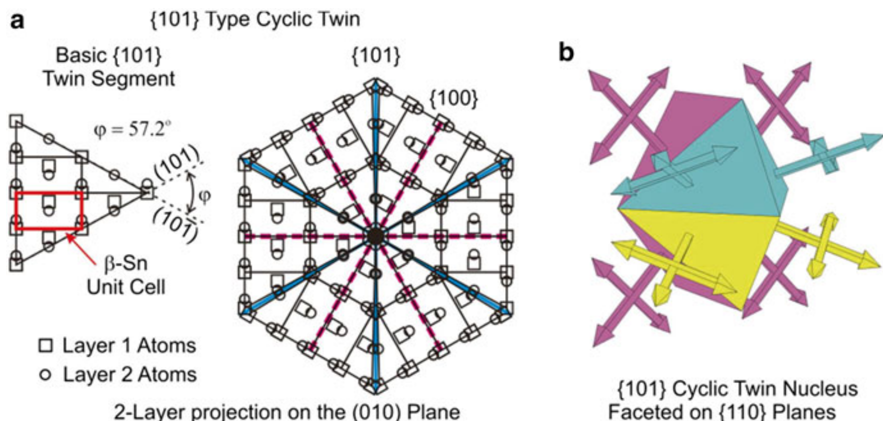

Fig. 4.8 Pseudo-hexagonal unit cell based on {101} cyclic twins made from tetragonal unit cells that form the basis of the beachball microstructure, and schematic arrangement of fast growing <110] planes that lead to stable growth of a cyclic (beachball) twin. [19]

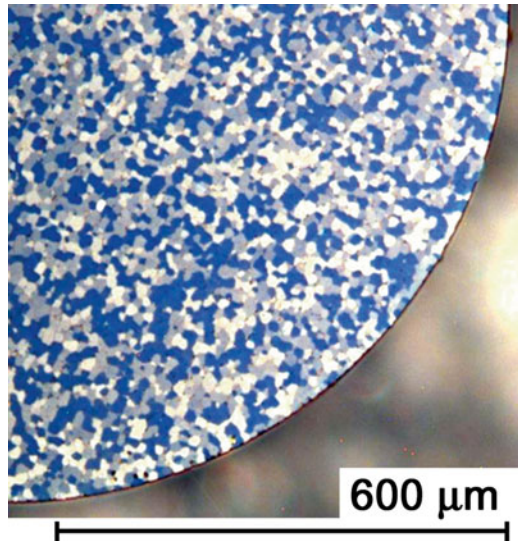

Fig. 4.9 Examples of joints in which solidification commenced at lower than usual temperatures, leading to an interlaced microstructure consisting of only there orientations

morphology will be maintained. With decreasing temperature, the most rapidly growing direction can shift to other directions, which has been documented in other crystal structures. Fast growth in directions other than (110) would not provide the stable growth of the same orientation in space, and hence, dendrites growing in other directions could intersect. This leads to interlaced microstructures, which still only have three orientations, but the cross section of this type of microstructure appears to have a fine polycrystalline appearance (example in Fig. 4.9). As the solidification rate slows down, conditions favoring normal [110] growth will often take over partway through the solidification process, and microstructures that show both the interlaced and beachball type microstructures signify that the initial solidification process occurred with greater undercooling. Also, with greater undercooling, it is more likely to obtain two nuclei, leading to rare examples of microstructures with 4 or 6 orientations, but these tend to occur about 1 % of the time.

It is common for these beachball twins to exhibit disorientations between 55 and 65° in EBSP maps such as the one shown in Fig. 4.5. Clearly, a 57° twin interface with periodic misfit dislocations could lead to a disorientation of 60°, but this boundary would have a higher energy than a perfect twin. Alternatively, some boundaries could have the lower energy 57° twin disorientation, but in order to close the cyclic twin, other boundaries would need to have a compensating 63° disorientation, and this has been observed in some locations in many joints, showing up as a double peak in the disorientation histogram. On the other hand, lattice curvature within each section of the cyclic twin could also allow *all* of the interfaces to have the 57° disorientation, such as the one shown in Fig. 4.5. As illustrated in the lower right c-axis crystal direction map the disorientation between the sections of the twinned grains are closer to 55°, as indicated by a blue line on a thicker black boundary line. There are only a couple of short segments near the center where a disorientation greater than 60° is present, and a disorientation just below 50° in the lower center

boundary. To compensate for the lack of closure of 57° twin boundaries, there are many low-angle boundaries present in large Sn grains (white boundaries in the lower right map). In some joints, there is a disorientation peak at 7°, which is an especially stable low-angle boundary that has a coincidence site lattice [21]; such a boundary is illustrated in Fig. 4.5 in the lower left section of the beachball, with a thicker white boundary. Inspection of the pole figures in Fig. 4.5 shows that all of the peaks are spread out by almost 10° along the great circle, indicating that each grain orientation is full of geometrically necessary dislocations, that allows the low energy 57° twin interfaces to exist. Consistent with the need to maintain 57° boundaries, the peak that is the least spread out is the common [100] rotation axis peak.

Twin Systems in Sn

There are two twin systems in tin [22]; the {101)<101] system that is involved with beachball nucleation, and the {301)<103] that is a mechanical twin system. Figure 4.10 illustrates the geometrical arrangement of one layer in the (010) plane

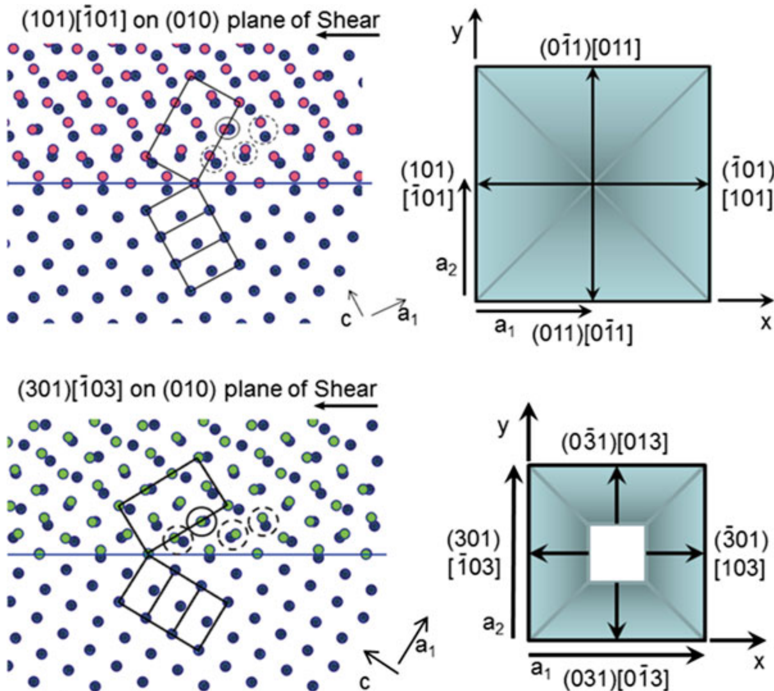

Fig. 4.10 Geometrical arrangement of Sn unit cells that lead to the {101} and {301}twin planes. Shear from the *dark to lighter* orientations could lead to the twin symmetry about the {101} or {301} plane. The *circled atom* positions illustrate the sense of shear and shuffles for each of the four repeating atom positions in the unit cell needed to generate the twin. Unit cells are plotted to show the four possible plane orientations and twin directions for each system

of shear (plane of the page). The second layer of the repeating crystal structure has atoms in the same arrangement but shifted in space from the corner to the body center position (see Fig. 4.8). Shear in the direction of the arrow is needed to generate either the pink {101) or green {301) atomic positions from the parent dark-blue positions. In both images, three parent unit cells are outlined to show the atom positions on a (010) face and to show the symmetric twin orientations in the twinned lattice. In both cases, only one out of 4 atoms is displaced in the direction of shear (circled with solid line), and 3 other atoms must shuffle to move to a new lattice position in the twinned crystal structure (circled with dashed lines). It is apparent that the shuffles are much larger in the {101) twin shear than in the {301) shear, and this may account for the fact that only {301) mechanical twins are observed. The geometrical arrangement of the four twin systems in each family are illustrated in the representations of 001 projections of the unit cell, showing the orientation of four sloped twin planes; the twin plane has a shallow slope from the basal plane for the {101) family and a steep slope for the {301) twins. The associated twin dislocation direction is shown on each plane (the magnitude of the twin Burgers vector is much smaller than the arrows). The presence of the {101) twins arises from the pseudo-hexagonal solidification nucleus. Thus, it is not likely that the twin interfaces that form on {101) planes are mobile, so their low energy makes these boundaries very stable. The {301) twins are commonly found in shock-deformed samples, and are not commonly observed in deformation conditions at lower strain rates.

Porosity

Solidification of metals always requires shrinkage, and there is a 2.3 % shrinkage from liquid to solid in Sn. The presence of a free surface on all sides of the solder ball provides a natural means for solidification shrinkage to be accommodated. However, larger pores often develop, particularly when solder paste is used, when pores containing flux are occasionally found at locations far from the outer surface. The associated outgassing caused by the flux evaporation are sometimes trapped inside the solder joint and are not able to escape during reflow process. The size of these pores varies from micron scale voids to sometimes a diameter of about ¼ the joint size. As solidification often commences at one of the two interfaces, and because the solidification front travels quickly, pores can be readily trapped in the solidified Sn, often near the substrate interface. Thus, it is important to control flux melting and flowing properties and a hold time below 200 °C allow for flux melting and activation, which accounts for the importance of the right reflow profile for each surface-mount and board assembly (see more detail in Chap. 2).

Porosity in solder joints also occurs at the scale of dendrites (a few microns), and this scale of porosity is occasionally observed on the surface of solder joints [23–26]. Surface porosity features near the interconnect on either side of the joint can lead to a local stress concentration due to the higher stress at the reduced diameter at the interconnect. In a recent study of porosity, X-ray tomographic reconstruction was

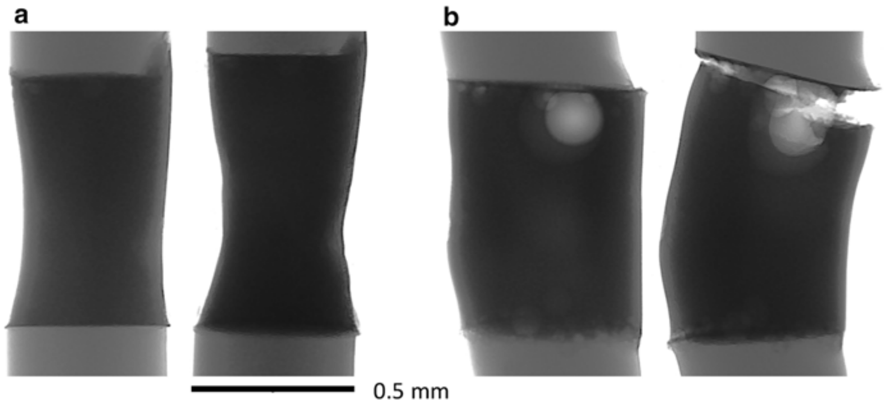

Fig. 4.11 Two radiographs of tensile samples of single crystal solder joints showing porosity on one interface in one joint (**b**) and none in the other (**a**). After tensile deformation to just past maximum load, the joint with pores developed a crack and a corresponding sudden load drop, while the one without pores deformed uniformly and did not exhibit a load drop

used to identify the locations of pores in a simple shear lap sample. In this investigation, computational simulation of the measured geometry including internal pores showed that large pores at the interface provided stress concentrations that facilitated damage development and crack initiation at the solder–substrate interface [23, 24]. However, microporosity arising from trapped voids in the interdendritic regions had no impact on properties. The effect of macroporosity is also visible in Fig. 4.11, which compares radiographs of two single-crystal cylinder type tensile solder joint (verified using X-ray diffraction). In the joint with several pores on one interface (Fig. 4.11b), the crack developed along the interface, while solder deformed more uniformly in the other joint with no pores (Fig. 4.11a).

The Effect of Microalloying

Microalloying of solder alloys (i.e., alloy additions less than 1 wt.%) provides a means to modify the properties of solder joints in beneficial ways [27–29]. One of the main motives for microalloying is to reduce the amount of undercooling that occurs prior to solidification, in order to obtain more homogeneous microstructures with less segregation of intermetallic phases. The IMC phases can grow quickly in the liquid state if they precipitate before Sn. In addition, microalloying to stimulate nucleation can lead to a polycrystalline microstructure, which is desirable for improved resistance to electromigration damage discussed later. A strategy for stimulating nucleation is with inoculants, i.e., to precipitate small compounds in the liquid that have a lattice spacing and surface energy that facilitates nucleation on Sn on this interface. The list of microalloying elements that have been investigated is

growing, but additions of Mn, Co, Cr, Al, Zn, Ni, Ge, RE elements, and POSS macromolecules have seen significant attention [27–38]. Some of these alloy additions have demonstrated significantly less undercooling but have not been necessarily effective in nucleating Sn. Many of these elements dissolve into the Cu_6Sn_5 intermetallic and alter the lattice parameters so that they have some effect on nucleation of Sn. For example, microalloying addition of Ni facilitates formation of fine $(Cu,Ni)_6Sn_5$ intermetallic particles that are effective in pinning grain boundaries and hence delay or prevent recrystallization (discussed in more detail later). Also, Ni additions alter the composition and growth rate of the intermetallic layer between the solder and the circuit attachment interfaces. Reduction of the IMC interfacial layer growth rate has generally been shown to be desirable because thicker brittle intermetallic materials are prone to cracking (also true with IMC particles within the Sn).

In addition to altering undercooling and the formation of precipitates with desirable characteristics, microalloying can affect the evolution of the interfacial intermetallic layers both during the melting stage and during joint service lifetime [39]. The small amount of microalloying from the surface finish can also affect the overall joint microstructure, as discussed in Chap. 2. The beneficial effects of Pd deposited in a thin layer on the interfacial metallurgy layers will be discussed later and also in Chap. 6. One of the most significant effects of the Cu in SAC alloys, in contrast to the binary Sn–Ag solder, is that the initial presence of Cu in the liquid solder alters the chemical potential of the liquid, so that there is less of a driving force for dissolution of Cu from the interfaces. This results in a smaller thickness of the brittle interfacial intermetallic layers, and when these layers are thinner, they are less prone to forming cracks. With less of a driving force for dissolution of Cu, there is less Cu in the liquid during the liquid stage, and consequently there is less supersaturation of the liquid with Cu that facilitates formation of large rods of Cu_6Sn_5, which can facilitate formation of cracks in the joint.

A third major effect of addition of Cu into the alloy in the first place is that it facilitates formation of cyclic twin tri-crystals. The presence of tri-crystals reduces the fraction of extreme values of the CTE among a population of joints. Figure 4.12 illustrates how formation of tri-crystals affects the average CTE from a population

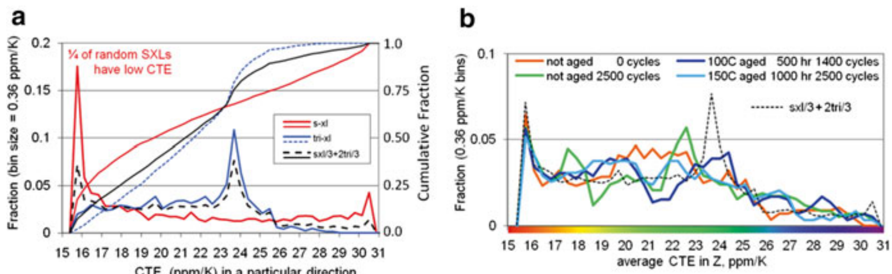

Fig. 4.12 Distribution of CTE values in a specified direction based upon a random number generated set of orientations. (**b**) Comparison with experimentally measured CTE values from a population of 200 joints. The experimental simulation is close to that expected when there is about 1/3 single crystal and 2/3 tricrystal joints

of about 2,000 simulated orientations based upon the assumption of a random orientation nucleation assumption, and many observations have shown that this assumption is close to what is observed in reality, as illustrated with several data sets with similar distributions [18].

This topic is in its infancy, and much more research and discovery are anticipated in the next decade. There is the opportunity and a general goal to identify microalloying elements that can truly make a random polycrystalline microstructure, or to assist in forming controlled crystal orientations that take advantage of the anisotropy of Sn in intentional ways.

The Effects of Isothermal Aging

The microstructure, mechanical response, property, and failure mechanisms of Sn-based solder joints are constantly changing due to the effects of isothermal aging. The observed variation in material behavior during thermal aging is universally detrimental to reliability and includes reductions in stiffness, yield stress, ultimate strength, and strain to failure, as well as highly accelerated creep. The reduction of tensile strength even with room temperature aging was identified in 1956 by Medvedev [40] in Sn–Pb solder, followed by many other publications in both Sn–Pb solder alloys and Sn–Ag and Sn–Ag–Cu alloy systems [41–50].

As the solidification microstructure is metastable, thermal activation will lead to microstructural evolution into structures with less interfacial energy and possibly changes in crystal structure of the IMCs. For example, Cu_6Sn_5 has a monoclinic microstructure in its equilibrium structure, but it initially forms in a metastable hexagonal structure that can transform into the monoclinic structure, depending on microalloying present in the alloy and thermomechanical history. Also, microalloying elements can stabilize the hexagonal structure [38].

Figure 4.13a, c illustrates the initial dendritic microstructure present after solidification on a finer scale than illustrated in Fig. 4.3. This microstructure has two constituents, particle-free Sn and regions surrounding it that contain dispersions of fine particles that are effective in pinning dislocations, leading to a composite material having hard regions and soft regions defined by the shapes of the primary β-Sn dendrites and the final liquid to solidify. Within the β dendrites, low-angle boundaries are commonly observed, which are visible in the backscattered electron image shown in Fig. 4.13c, (small orientation differences lead to large differences in the backscattered electron intensity). With optimized tilting conditions, individual dislocations or dislocation subgrain walls can be visualized. In the midst of the nanoscale Ag_3Sn precipitates, some of the larger particles have other compositions, depending on the initial solder composition and the time and temperature history in the liquid state. There are many variations on this microstructure, depending on the Ag content and the rate of solidification. With a slower solidification rate, such as in larger sample volumes (e.g., cast bulk tensile samples), the Ag_3Sn particles are larger and more cylindrical than spherical, and the dendritic structure is more clearly defined [51].

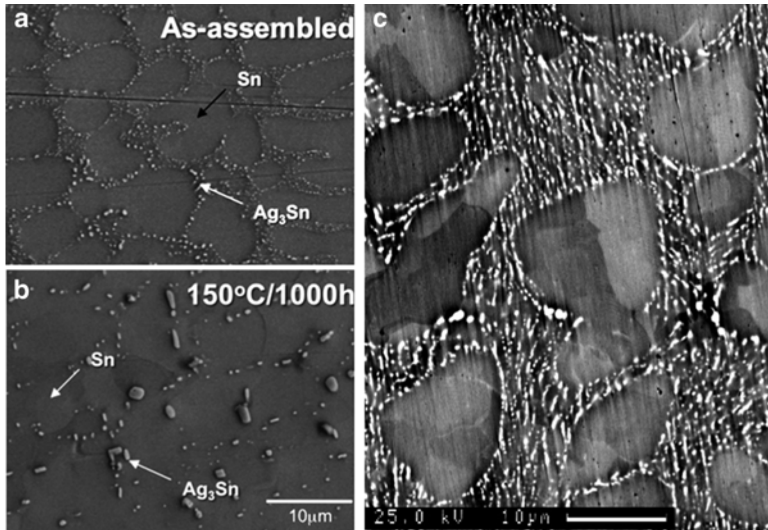

Fig. 4.13 Secondary electron image of as-fabricated SAC305 solder microstructure (**a**), and the coarsened microstructure after aging (**b**). Backscattered electron micrograph of as-solidified eutectic Sn–Ag solder (**c**) illustrating subgrain boundaries within β tin dendrites, which are only slightly visible in the secondary electron images in (**b**) [Photo credit Tae-kyu Lee (**a, b**) and Boon-Chai Ng (**c**)]

Effect of Aging on Precipitate Morphology

It is common to simulate the microstructure that develops with years of service conditions by aging an as-fabricated sample to transform the eutectic microstructure regions into Sn with roughly evenly distributed larger particles (Fig. 4.13b). The presence of dislocations within the β-Sn dendrite provide dislocation pipes that facilitate coarsening of Ag_3Sn particles. This coarsening process results in an increase in the spacing between particles and hence a reduction in the stress needed to cause dislocation motion throughout the joint. In thermal cycling experiments on as-fabricated samples, this drop in the stress occurs exponentially over the first several hundred cycles, and it depends on the magnitude of strain. While aging can also cause coarsening similar to that observed in thermal cycling experiments, the significant difference is that during thermal cycling, the stress changes continually, leading to dislocation generation and recovery, and the temperature change facilitates the dissolution of precipitates at high temperature and re-precipitation of dissolved elements in solution back onto existing precipitates, which is a process that does not occur during long-term aging. Hence, interpretation of outcomes of experiments with an isothermally aged microstructure needs to be interpreted with these differences in mind.

The strength degradation and the increase in creep rate with the isothermal aging temperature are interrelated. The underlying mechanism for the reduction in strength

in SAC solder alloys after aging is due the microstructure coarsening and also the IMC precipitate coarsening. With the temperature increase that starts the aging process, there is stress relaxation arising from CTE and anisotropic stiffness effects, resulting in an exponentially decreasing creep rate. Creep is strongly dependent on dislocation nucleation, mobility, and grain size. Finer grains will cause more grain boundary sliding facilitated by absorption of dislocations into boundaries, which accelerates grain boundary diffusion and thus leads to faster creep deformation and stress relaxation. Particle coarsening results in larger distances between particles, which enables more shear strain by bowing of dislocations that are pinned by particles. With fewer and larger particles, the pinning effect of particles on grain boundary motion is reduced. The contribution of dislocation motion to the apparent elastic modulus will therefore increase with increasing grain and particle size. This explains why isothermal aging can cause a reduction in the apparent elastic modulus [50]. The interrelationships between particle spacing, dislocation density and grain boundary mobility will be discussed in more depth in Chap. 5.

Isothermal aging results also show that after an initial tensile strength drop, Sn–Pb eutectic solder reaches a relatively stable condition after about 200 h of aging. However, for SAC, both the tensile and creep properties continuously change with increasing aging time. It is noteworthy that the creep deformation of SAC is only lower (better than) Sn–Pb at room temperature and shorter aging times. There is a crossover point at about 50 h of aging at 125 °C (Fig. 4.14) where the creep resistance of SAC becomes lower than Sn–Pb [49, 52]. The associated microstructure comparison between the Sn–Pb and the SAC305 alloy is shown in Fig. 4.15. But we must note that these results were based on bulk solder samples. The situation becomes more complex when we consider the joint as an interconnect with different interface materials.

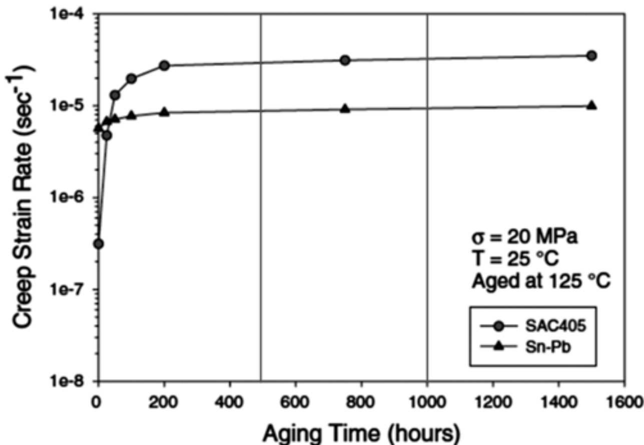

Fig. 4.14 Comparison of Sn–Pb and SAC405 creep rates for aging at 125 °C

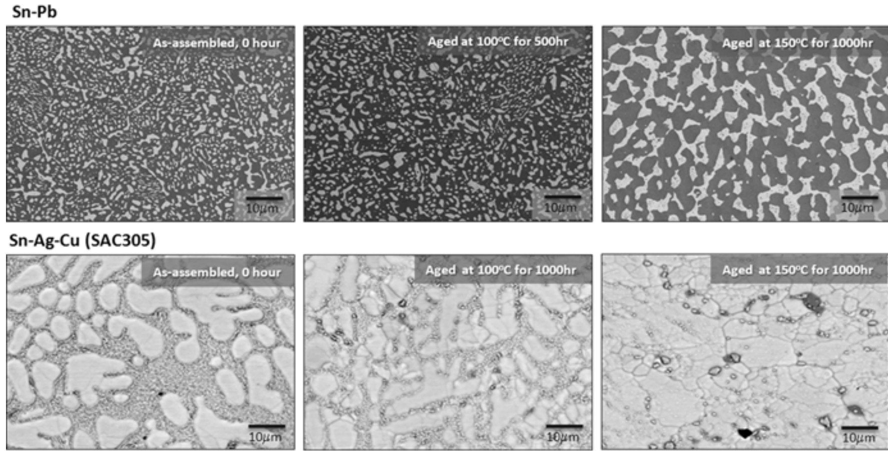

Fig. 4.15 Microstructure comparison of Sn–Pb and SAC305 before and after aging at 100 and 150 °C for 500–1,000 h

Interfacial Composition and Property Evolution with Aging

Isothermal aging is also affected by alloying element concentration gradients. The rate of particle growth depends on the precipitation and coarsening kinetics, which in turn depend on the local concentration gradients. In thermal cycling conditions, coarsening is also affected by dislocation generation and stress states, but in either case, variability is expected because diffusivity in Sn is anisotropic (Table 4.1). As each joint has its own orientation, the details of particle coarsening vary according to the crystal orientation and the stress state boundary conditions arising from the interactions between the crystal orientation, the package design, and the position of the joint in the package.

As electronic components evolve to smaller and higher functionality with higher-density packages, the solder ball diameter needs to shrink [53, 54]. This technological trend is associated with several challenges because as the solder joints become smaller, the thickness and morphology of the solder joint interface intermetallic compounds (IMC) will become a larger fraction of the volume of the interconnect. The related concentration gradients will depend more sensitively on the composition of the bulk solder alloy, the microstructure, and the surface finish of the packages and boards [55–57]. One of the main sources for the alloy element concentration gradient is the package and board-side surface finish. Since the component and board experience a liquid–solid diffusion interface during reflow, a significant amount of elements from the surface finish flow into the bulk liquid solder and sometimes produce a localized element concentration, which can be observed by identifying the IMC precipitate composition and location. The influence of these surface-preserving layers on joint properties is stronger with smaller joints.

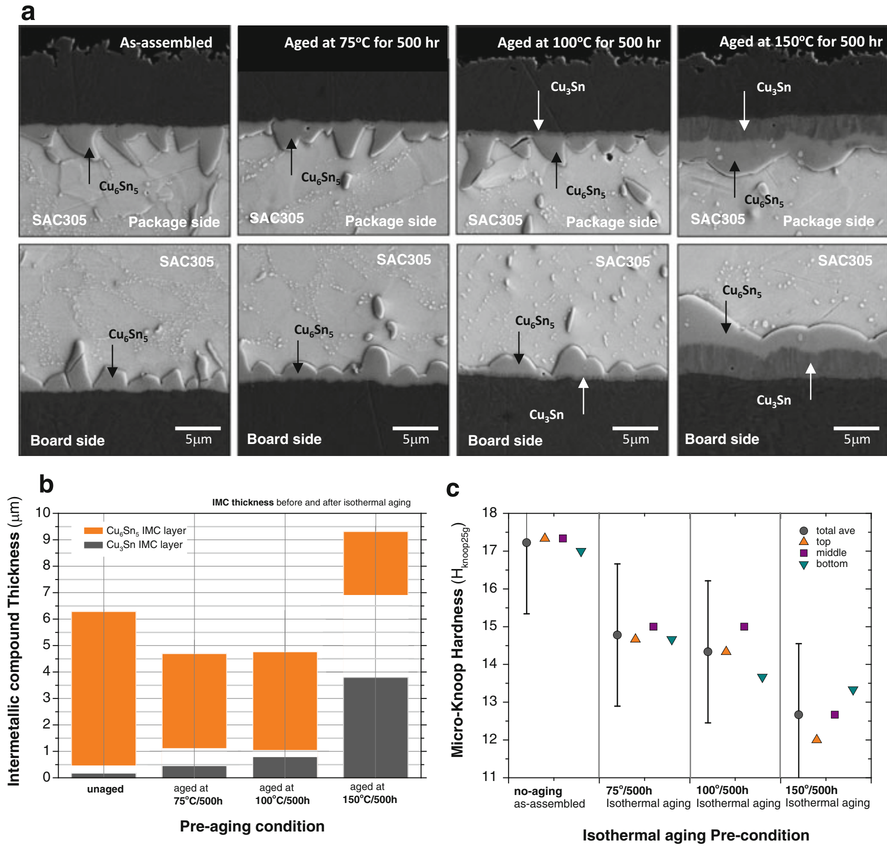

Fig. 4.16 Effect of temperature on SEM microstructure, IMC thickenss, and hardness before and after isothermal aging in a joint with Immersion Sn surface finish on the package side and Cu–OSP on the board side (**a**). Package side (*top*) and board side (*bottom*) interfaces have similar microstructures after aging for 500 h at 75, 100, or 150 °C. The IMC thickness increases (**b**) and Micro Knoop hardness decreases (**c**) with increasing temperature

As discussed in Chap. 2, various surface finish combinations can exist on either side of a joint. For example, when both sides of the joint use organic solderability preservative (OSP) on Cu, Fig. 4.16 shows the same features on both sides of the joint. As explained in Chap. 2, OSP is an organic layer and dissolves into the solder joint during reflow, leaving the joint interface with a simple Cu/IMC/solder interface. When the composition is similar on both sides but made with different methodologies, such as immersion Sn surface finish on Cu and OSP surface finish on the other side, with SAC305 solder between, the feature characteristics are the same on both sides of the joint (compare with Fig. 2.9). While the morphology of the Cu_6Sn_5 differs, a relatively balanced elemental gradient will exist on both sides of the joint; a scallop-shaped IMC develops with a finely distributed IMC precipitate network in the bulk. With isothermal aging, as shown in Fig. 4.16, the scallop shaped IMC layers

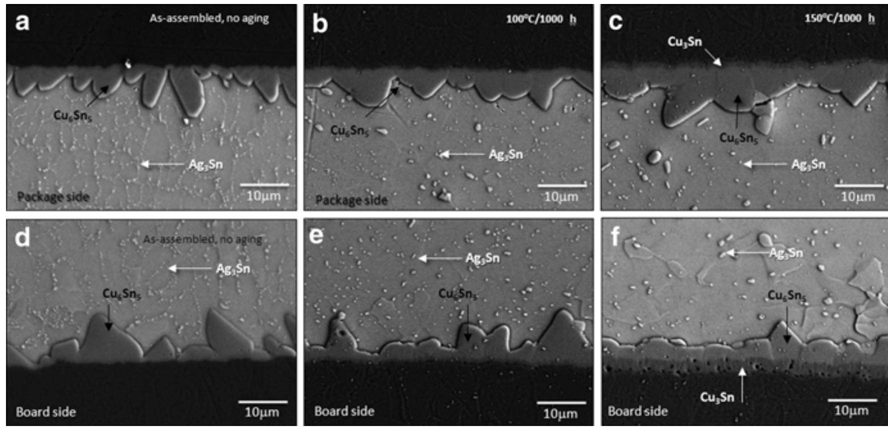

Fig. 4.17 Effect of aging time on SEM microstructure for Cu–OSP surface finished package side (a,b,c) and Cu–OSP on the board side (d,e,f) before and after isothermal aging. Package side interface (**a, d**) as-assembled (**b, e**) after 100 °C/1,000 h aging and (**c, f**) after 150 °C/1,000 h aging [13]

on the package-side and board-side interface change from at the initial state to develop a more uniform thickness after aging at 150 °C. This smoothing is also shown in the IMC thickness plot in Fig. 4.16b, and in Fig. 4.17b, e, where the gap between the maximum and minimum thickness of the Cu_6Sn_5 layer becomes narrower after aging at 150 °C for 500. With increasing time, the overall thickness variation becomes less and a uniform thickness develops. The growth of the Cu_3Sn layer is also observed with a gradual growth rate, but the growth is accelerated with higher aging temperature. Because both package and board side have a sufficient source of Cu, the microstructure and hardness difference between the package side and board side is minimal. Figure 4.16c shows similar hardness values at different positions in the joint, but an overall decrease of hardness occurs due to the bulk microstructure evolution with larger IMC precipitates. Figure 4.17 also shows the same kind of interface microstructure development when both joints have the same Cu-OSP surface preparation.

Unlike Cu/solder/Cu structures, when one surface has Ni/Au surface finish, (either electrolytic Ni/Au or electroless Ni/Au (ENIG)), a more complicated structure develops with aging. The formation and the growth mechanisms of IMCs that form between the solder and the interfacial metallization have been extensively studied in various solder alloy systems and alloy compositions [58–62]. During thermal aging, the IMC on the Ni side will grow with a substantial morphology change from $(Cu,Ni)_6Sn_5$ needles to a smoother continuous morphology while suppressing the growth of the Cu_3Sn layer.

One example with electrolytic Ni/Au surface finish is shown in Fig. 4.18, where the microstructure of two different solder alloys, Sn-1.0Ag-0.5Cu (wt.%) (SAC105) and Sn-3.0Ag-0.5Cu (wt.%) (SAC305), are compared. SAC305 shows finer and

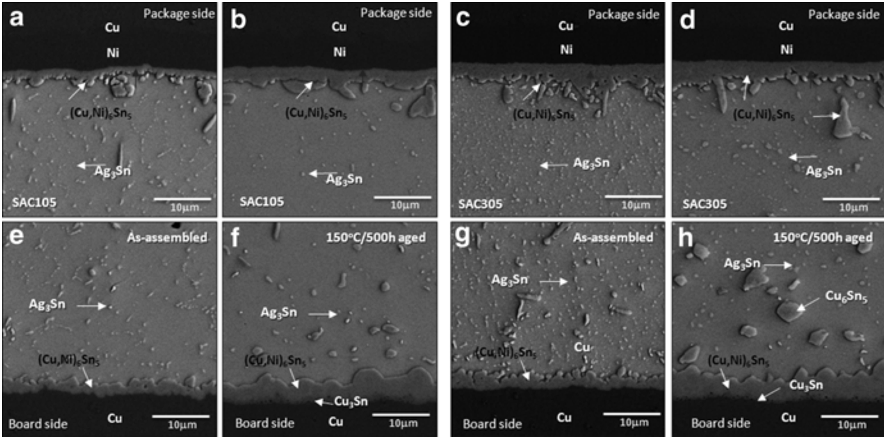

Fig. 4.18 Effect of alloy composition on SEM cross-section microstructure on the package side (**a, b, c, d**) and board side (**e, f, g, h**) of SAC105 (**a, b, e, f**) and SAC 305 (**c, d, g, h**) before aging (**a, e, c, g**) and (**b, f, d, h**) after aging at 150 °C/500 h

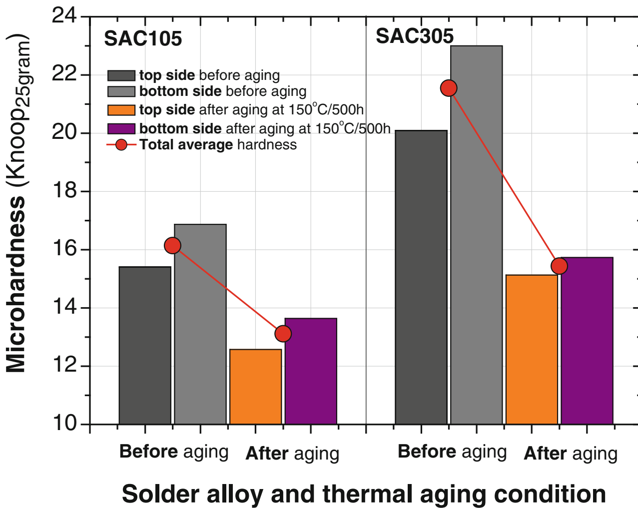

Fig. 4.19 Micro knoop hardness data for SAC105 and SAC305 before and after aging at 150 °C/500 h

more abundant Ag_3Sn precipitates in the solder β-Sn matrix than SAC105, which eventually makes SAC305 harder compared to SAC105 joints. The measured hardness in Fig. 4.19 shows how much the hardness drops after isothermal aging, which is based on 12 solder joints per condition with two indentations per joint inside the solder bulk region, near-package-side interface, and board-side interface. The IMC precipitates grew larger, and the number of precipitates decreased, resulting in a

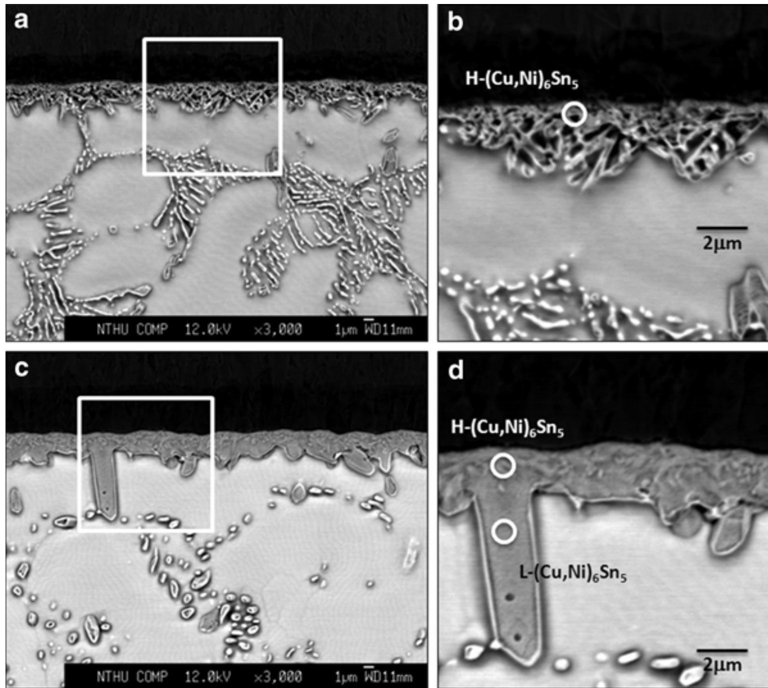

Fig. 4.20 Package side interface after board assembly (**a, b**) and after isothermal aging (**c, d**). Electrolytic NiAu surface finish

lower hardness value after aging. The drop in hardness is smaller in SAC105 since the initial amount of Ag_3Sn is lower than SAC305. Also, the interface IMC layer becomes smoother after aging compared to the Cu/solder/Cu joint configuration, but with a closer look at the interface structure, there are actually two distinguishable layers discussed next.

Figure 4.20 shows an interface between SAC305 solder and electrolytic Ni/Au surface after assembly and after isothermal aging at 150 °C for 500 h. Actually Fig. 4.20a is the same interface which was shown in Fig. 2.9. As explained in Chap. 2 already, during reflow, a reaction between the solder alloy SAC305 and the Ni/Au interface occurred with Ni diffused from the substrate side into the solder alloy, leading to the formation of needle-like $(Cu,Ni)_6Sn_5$ at the solder/Ni interface. The composition analysis using EPMA shows that the average Ni concentration was ~20.0 at.% in $(Cu,Ni)_6Sn_5$, represented as H-$(Cu,Ni)_6Sn_5$ in Fig. 4.20b. After aging, an additional layer covered the initial IMC layer at the solder/Ni interface, and two kinds of $(Cu,Ni)_6Sn_5$ layers with different Ni content were detected. Figure 4.20d shows that a continuous L-$(Cu,Ni)_6Sn_5$ layer with a lower Ni content formed above the H-$(Cu,Ni)_6Sn_5$ IMC, proving that the Ni is distributed nonuniformly in $(Cu,Ni)_6Sn_5$ and maintains a sharp interface between those two. In H-$(Cu,Ni)_6Sn_5$,

the average Ni concentration was similar to the as-assembled interface with ~16.7 at.% Ni while after aging it was ~6.4 at.% in L-$(Cu,Ni)_6Sn_5$. The $(Cu,Ni)_6Sn_5$ IMC formation is attributed to the redistribution of Ni and Cu atoms as the Ni substrate reacts with SAC305 solder. As $(Cu,Ni)_6Sn_5$ is more stable than Cu_6Sn_5 [4], apparently the H-$(Cu,Ni)_6Sn_5$ cannot be diluted with subsequent aging, which resulted in an interface between the H-$(Cu,Ni)_6Sn_5$ and L-$(Cu,Ni)_6Sn_5$. During aging, the solubility of Cu in Sn decreases from 1.23 wt.% to approximately 0.001 wt.% as temperatures change from 250 to 150 °C [9]. This quantitative analysis shows that the Cu content near the solder/Ni interface decreased from 1.17 wt.% as reflowed to 0.46 wt.% after aging. Thus, the supersaturated Cu gradually migrated toward the interface and precipitated as L-$(Cu,Ni)_6Sn_5$ at the interface to decrease the energy of the system. Hence, L-$(Cu,Ni)_6Sn_5$ formed a substantial layer above the H-$(Cu,Ni)_6Sn_5$ IMC during aging [31]. In addition, H-$(Cu,Ni)_6Sn_5$ is as an effective diffusion barrier to block the Ni migration into solder, and retarding Ni diffusion into L-$(Cu,Ni)_6Sn_5$.

ENIG Versus ENEPIG After Isothermal Aging

An even more subtle example of the importance of microalloying can be illustrated by adding an additional element into consideration to show how it causes differences in the evolution of the IMC layer that can significantly affect interfacial properties. As reviewed in Chap. 2, electroless nickel immersion gold (ENIG) is aformed by the deposition of electroless nickel–phosphorus on a catalyzed copper surface followed by a thin layer of immersion gold. The immersion gold protects the underlying nickel from oxidation/passivation like the electrolytic Ni/Au surface finish [63, 64]. One of the drawbacks with ENIG is the potential risk of galvanic hypercorrosion in the Ni–P layer caused by the immersion in the Au solution, which is usually called the "black pad" issue [65]. To overcome, an additional layer was introduced, and the ENIG becomes electroless nickel/electroless palladium/immersion gold (ENEPIG) surface finish. The insertion of the Pd layer is believed to prevent corrosion underneath the Ni–P layer that exists before the immersion Au plating solution is used.

The growth behavior of Cu_6Sn_5 in ENIG and ENEPIG joints in Fig. 2.12 shows differences in the interfacial reaction of ENIG and ENEPIG solder joints. Irregular-shaped IMCs formed after reflow on both metallizations. During the early stage of soldering, the thin Pd finish as well as the Au finish was dissolved within a few seconds into solder [66].

Figure 4.21 shows the interfacial reaction of ENIG and ENEPIG solder joints followed by thermal aging. After a 1,000 h 150 °C thermal age, the morphology of the IMC became layer-like in both joints. After aging, a thin dark layer formed between the Ni–P and Cu–Sn IMC in both samples (Fig. 4.21a, b). The composition of this phase was 75.4 at.% Ni and 24.6 at.% P, (Ni_3P) that precipitated from amor-

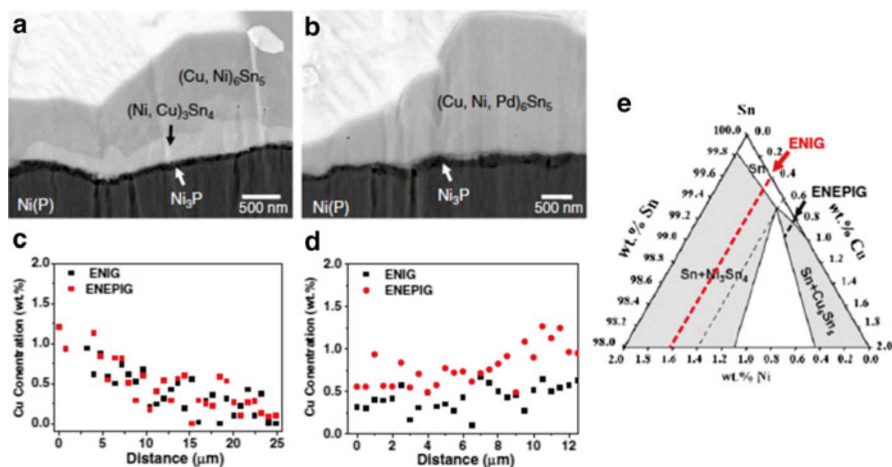

Fig. 4.21 Detailed cross-sectional images. (**a**) ENIG and (**b**) ENEPIG after 1,000 h aging; concentration profiles of Cu trace line near the solder/IMC diffusion zone in (**c**) vertical and (**d**) parallel directions and (**e**) enlarged Sn corner of Sn–Cu–Ni ternary isotherm [31]

phous electroless Ni–P during the reflow process [63, 64, 67, 68]. The formation of an IMC layer on the Ni–P layer would motivate the Ni_3P crystallization. Interestingly, an additional IMC formed between Ni_3P and $(Cu,Ni)_6Sn_5$ in the ENIG joint with a bright phase in Fig. 4.21a but not in the aged ENEPIG joints. The composition of the bright IMC was 36.4 at.% Ni, 10.7 at.% Cu, and 53.0 at.% Sn, which is close to the stoichiometry of $(Ni,Cu)_3Sn_4$. The inclusion of Cu in this compound that normally forms on Ni sites comes from the Cu in the solder. From the Sn–Cu–Ni ternary isotherm [69–71], the $(Cu,Ni)_6Sn_5$ IMC is stable when the Cu concentration in the Sn–Cu–Ni alloy is greater than 0.6 wt.%. This implies that the bright layer formed when the Cu content was less than 0.6 wt.%. Figure 4.21c shows the concentration of the Cu with distance from the interface toward the solder side in a direction perpendicular to the interface. It is evident that the concentration of Cu decreased from interface into the solder, indicating that Cu migrated to the solder/IMC interface during thermal aging to grow Cu_6Sn_5. The other Cu composition trace in Fig. 4.21d was measured at distance of 2 µm above interface, indicating fairly constant values for both conditions, yielding an average Cu concentration of 0.4 ± 0.2 wt.% and 0.8 ± 0.5 wt.% for ENIG and ENEPIG joints, respectively. As indicated in Fig. 4.21e, only $(Cu,Ni,Pd)_6Sn_5$ formed at the solder/ENEPIG interface due to the higher Cu concentration, and the smaller Cu concentration (0.4 wt.%) required $(Ni,Cu)_3Sn_4$ to form between $(Cu,Ni)_6Sn_5$ and Ni_3P layer. The higher Cu concentration in the ENEPIG joint can be attributed to less growth of interfacial $(Cu,Ni,Pd)_6Sn_5$. This difference provided the ENEPIG, a potentially tougher mechanical interface than ENIG joint structures, which can show improved mechanical stability. The example of the effect of microalloying Pd in the solder via surface

finish illustrates how composition and chemical reaction evolution is a crucial factor to consider in order to assure the stability of the joint in thermal, mechanical, and chemical performance. Clearly, the structure of the IMC geometry can affect the performance, the elemental distribution, as shown in this case where the local Cu concentration affects the stability of the interface, which then affects the overall property of the joint.

Summary

The formation of a solder joint involves complex nonequilibrium conditions resulting from many factors. First, the reluctance of β Sn to generate a stable nucleus leads to formation of single-crystal or tri-crystal (twinned) joints in the SAC alloy system and a solidified state that has a high defect density due to the fast growth rate of the solid. This characteristic is sensitive to both alloy and microalloying chemistry, and the details of solidification will differ according to details of the alloy additions. Secondly, once solidified, which occurs within a second, there is not much time for equilibrating complex internal stress states arising from the anisotropic CTE and elastic moduli of Sn. Thus, dislocation activity is substantial, resulting in orientation gradients and some generation of subgrains. Thirdly, the intermetallic precipitate and interface structure is heterogeneous, and it evolves with aging to weaken the microstructure. These are important issues that affect the performance of the joint in thermal and mechanical fatigue conditions that are discussed further in Chaps. 5 and 6.

Aging also causes complex restructuring and growth of the IMC layer that depends on the history and chemistry of joint formation with the metallization layers on either side of the joint. The necessary and complex metallization includes thin layers that result in localized microalloying. When strategically managed, this form of microalloying can lead to desirable IMC properties that are important, as its strength and toughness significantly affect joint properties discussed further in Chap. 6. However, before considering the importance of IMC properties, Chap. 5 examines how the very unstable solidification microstructure evolves under the influence of thermal cycling. With thermal cycling, the effects of aging discussed in the last part of this chapter take place, but it is further complicated by temperature changes that also introduce energy into the microstructure by elastic and plastic straining coupled with changes in solubility and diffusivity. These compositional and strain energy changes create driving forces for atomic transport that promotes significant changes in the microstructure, and hence, significant changes in joint properties that are explored in the next chapters. An illustrated overall summary chart is shown in Fig. 4.22.

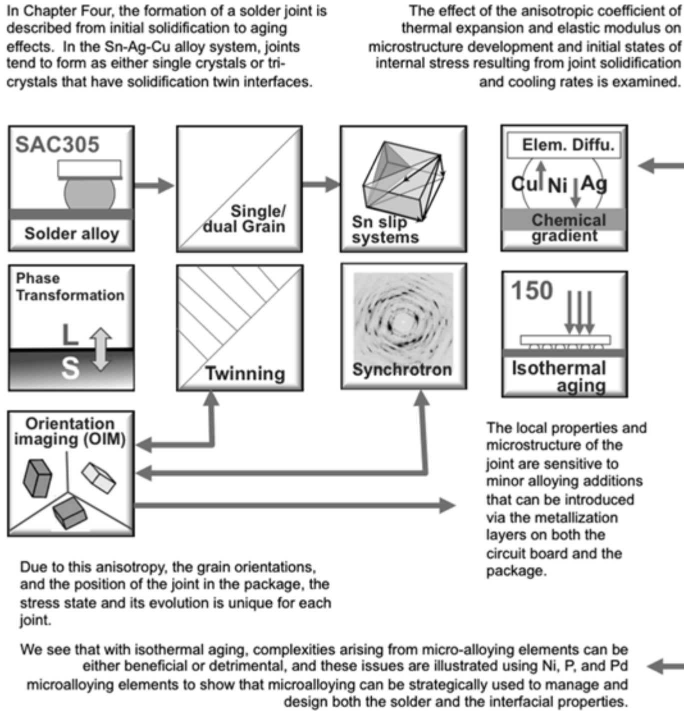

Fig. 4.22 Overall summary chart of Chap. 4

References

1. Y. S. Huang, H. Y. Hsiao, C. Chen, K. N. Tu, The effect of a concentration gradient on interfacial reactions in microburaps of Ni/SnAg/Cu during liquid-state soldering, Scripta Materialia, vol.66(10), pp. 741-744, 2012.
2. M. S. Park, R. Arroyave, Early stages of intermetallic compound formation and growth during lead-free soldering, ACTA materialia, vol. 58(14), 4900–4910, 2010.
3. Chung, C. Key, Y. J. Chen, Yang, T. L., Kao, C. R., Reactions of Sn-4.0Ag-0.5Cu on Cu and Electroless Ni Substrate in Premelting Soldering Process, Journal of Electronic Materials, vol.42(6), pp.1254–1259, 2013.
4. L. Liu, T.-C. Liu, Y.-S. Huang, C. Chen, Concentration Gradient of Ni in Reduced SnAg Thickness in Ni/SnAg/Cu Microbumps during Solid-State Aging, Ecs Solid State Letters V.2 (2), pp.15–18, 2013.
5. T. Wang, X. Chen, G.-Q. Lu, G.-Y..Lei, Low-temperature sintering with nano-silver paste in die-attached interconnection, Journal of Electronic Material, V. 36 (10), pp. 1333-1340, 2007.
6. M. Maruyama, R. Matsubayashi, H. Iwakuro, S. Isoda, T. Komatsu, Silver nanosintering: a lead-free alternative to soldering, Applied Physics A-Materials Science & Processing V. 93(2), pp.467–470, 2008.
7. K. S. Siow, Mechanical properties of nano-silver joints as die attach materials, Journal of alloys and compounds, vol.514, pp.6–19, 2012.
8. N. S. Bosco, F. W. Zok, Critical interlayer thickness for transient liquid phase bonding in the Cu-Sn system, Acta Materialia V. 52(10), pp. 2965-2972, JUN 7 2004

9. J. F. Li, P. A. Agyakwa, C. M. Johnson, Interfacial reaction in Cu/Sn/Cu system during the transient liquid phase soldering process, Acta Materialia V. 59(3), pp. 1198-1211, 2011.
10. W. D. Brown, S. S. Ang, H. A. Mustain, Transient Liquid Phase Die Attach for High-Temperature Silicon Carbide Power Devices, IEEE Transactions on Components And Packaging technologies, V.33(3), pp. 563–570, 2010.
11. D. G. House, E.V. Vernon, Determination of The Elastic Moduli of Tin Single Crystals, and their Variation with Temperature, British Journal of Applied Physics, V.11, 254–259, 1960.
12. J. A. Rayne, B.S. Chandrasekhar, Elastic Constants of Beta-Tin from 4.2-Degrees-K To 300-Degrees-K, Physical Review, V. 118, pp.1545–49, 1960.
13. V. T. Deshpande, D. B. Sirdeshmukh, Thermal Expansion of Tin in Beta-Gamma Transition Region, Acta Cryst. V. 15, pp.294–295, 1962.
14. B. Zhou, T. R. Bieler, G. Wu, S. Zaefferer, T.-K. Lee, K.-C. Liu, In-Situ Synchrotron Characterization of Melting, Dissolution and Resolidification in Lead-Free Solders, Journal of Electronic Materials, V.41(2), pp.262–272, 2012.
15. B. Zhou, T. R. Bieler, G. Wu, S. Zaefferer, T.-K. Lee, K.-C. Liu, In-Situ Synchrotron Characterization of Melting, Dissolution and Resolidification in Lead-Free Solders, Journal of Electronic Materials, V. 41(2), pp. 262–272, 2012.
16. T.-K. Lee, B. Zhou, L. Blair, K.-C. Liu, T. R. Bieler, Sn-Ag-Cu solder joint microstructure and orientation evolution as a function of position and thermal cycles in ball grid arrays using Orientation Imaging Microscopy, Journal of Electronic Materials, V.39(12), pp. 2588-97, 2010.
17. T.K. Lee, W. Xie, Bite Zhou, T. R. Bieler, K,-C, Liu, Impact of Isothermal Aging on Long-Term Reliability of Fine-Pitch Ball Grid Array Packages with Sn-Ag-Cu Solder Interconnects: Die Size Effects, J. Electronic Materials, V.40(9), pp. 1967–76, 2011.
18. T. R. Bieler, B. Zhou, L. Blair, A. Zamiri, P. Darbandi, F. Pourboghrat, T.-K. Lee, K.-C. Liu, The Role of Elastic and Plastic Anisotropy of Sn on Recrystallization and Damage Evolution During Thermal Cycling in SAC305 Solder Joints, Journal of Electronic Materials, V. 41(2), pp.283–301, 2012.
19. L.P. Lehman, Y. Xing, T.R. Bieler, E.J. Cotts, Cyclic twin nucleation in tin-based solder alloys, Acta Materialia, V.58, pp.3546–3556, 2010.
20. B. Arfaei, N. Kim, and E.J. Cotts, Dependence of Sn Grain Morphology of Sn-Ag-Cu Solder on Solidification Temperature, Journal of Electronic Materials, Vol. 41(2), pp.362–74, 2012.
21. A. U. Telang, T. R. Bieler, M.A. Crimp, Grain Boundary Sliding on near-7, 14, and 22º Special Boundaries During Thermomechanical Cycling in Surface-Mount Lead-Free Solder Joint Specimens, Materials Science and Engineering, A421 (1-2),pp. 22–34, 2006.
22. K. N. Tu, D. Turnbull, Direct Observation Of Twinning In Tin Lamellae, Acta Metallurgica, Vol. 18, pp. 915–929, 1970.
23. E. Padilla, V. Jakkali, L. Jiang, N. Chawla, Quantifying the effect of porosity on the evolution of deformation and damage in Sn-based solder joints by X-ray microtomography and microstructure-based finite element modeling, Acta Mater. V.60(9), pp.4017–4026, 2012.
24. M. A. Dudek, L. Hunter, S. Kranz, J. J. Williams, S. H. Lau, N. Chawla, Three-dimensional (3D) visualization of reflow porosity and modeling of deformation in Pb-free solder joints, Materials Characterization V. 61(4), pp.433–439, 2010.
25. Y. C. Xie, D. J. Lai, J.K.L. Chan, Experimental studies of pore formation in surface mount solder joints, Materials Science and Engineering B, V. 38 (1-2), pp. 53–61, 1996.
26. Q. Yu, T. Shibutani, D.-S. Kim, Y. Kobayashi, J. Yang, M. Shiratori, Effect of process-induced voids on isothermal fatigue resistance of CSP lead-free solder joints, Microelectronics Reliability, V.48, pp.431–437, 2008.
27. I. E. Anderson, J. W. Walleser, J. L. Harringa, F. Laabs, A. Kracher, Nucleation Control and Thermal Aging Resistance of Near-Eutectic Sn-Ag-Cu-X Solder Joints by Alloy, Journal of Electronic Materials, V. 38(12) pp. 2770–2779, 2009
28. I. E. Anderson, Boesenberg, A. J. L. Harringa, D. Riegner, A. Steinmetz, D. Hillman, Comparison of Extensive Thermal Cycling Effects on Microstructure Development in Micro-alloyed Sn-Ag-Cu Solder Joints Anderson, Journal of Electronic Materials, V.41(2), pp.390–396, 2012.
29. N. Huang, A. M. Hu, M. Li, D. L. Mao, Influence of Cr alloying on the oxidation resistance of Sn-8Zn-3Bi solders, Journal of Materials Science-Materials in Electronics, V24(8), pp.2812–2817, 2013.

30. W. Liu and N.-C. Lee, The Effects of Additives to SnAgCu Alloys on Microstructure and Drop Impact Reliability of Solder Joints, JOM 59, pp.26–31 2007.
31. C.-F. Tseng, T.-K. Lee, G. Ramakrishna, K.-C. Liu, J.-G. Duh, Suppressing Ni_3Sn_4 formation in the Sn–Ag–Cu solder joints with Ni–P/Pd/Au surface finish, Materials Letters, V. 65, pp.3216–3218, 2011.
32. S.-W. Fu, C.-Y. Yu, T.-K. Lee, K.-C. Liu, J.-G. Duh, Impact crack propagation through the dual-phased $(Cu,Ni)_6Sn_5$ layer in Sn-Ag-Cu/Ni solder joints, Materials Letters, V. 80(1), 103–105, 2012
33. T.-K. Lee, B. Zhou, T. Bieler, C.-F. Tseng, J.-G. Duh, Characterization of recrystallization and microstructure evolution in lead-free solder joints using EBSD and 3D-XRD, Journal of Electronic Materials (JEM), V.42 (2), pp.215–223, 2013
34. H. Choi, T.-K. Lee, Y. Kim, H. Kwon, C.-F. Tseng, J.-G. Duh, H. Choe, Improved strength of boron-doped Sn-1.0Ag-0.5Cu solder joints under aging conditions, Intermetallics, V.20 (1), pp.155–159, 2012
35. C.-Y. Yu, T.-K. Lee, M. Tsai, K.-C. Liu, J.-G. Duh, Effects of Minor Ni Doping on Microstructural Variations and Interfacial Reactions in Cu/Sn-3.0Ag-0.5Cu-xNi/Au/Ni Sandwich Structures, Journal of Electronic Materials (JEM), V.39 (12), pp.2544–2552, 2010
36. G. Chen, Y. W. Shi, Z. D. Xia, Y.F. Yan, Study on the Microstructure of a Novel Lead-Free Solder Alloy SnAgCu-RE and Its Soldered Joints, Journal of Electronic Materials, V.31 (10), 1122, 2002
37. L. Andre, K.N. Subramanian, Development of Nano-Composite Lead-Free Electronic Solders, Journal of Electronic Materials, V.34 (11), pp.1399–1405, 2005
38. K. Nogitaa, T. Nishimura, Nickel-stabilized hexagonal $(Cu, Ni)_6Sn_5$ in Sn–Cu–Ni lead-free solder alloys, Scripta Materialia, V.59, pp.191-194, 2008
39. G. Ghosh, Dissolution and interfacial reactions of thin-film Ti/Ni/Ag metallization in solder joints, Acta Materialia, V.49(14), pp.2609–2624, 2001.
40. A. S. Medvedev, Aging of Tin-Lead Solders and Joints Soldered by Them, Metallovedenie i Obrabotka Metallov, No.7, pp. 16–23, 1956.
41. C. M. Chuang, T. S. Lui, L. H. Chen, Effect of aluminum addition on tensile properties of naturally aged Sn-9Zn eutectic solder, Journal of Materials Science, V.37(1), pp.191–195, 2002.
42. Q. Xiao, H. J. Bailey, W. D. Armstrong, Aging Effects on Microstructure and Tensile Property of Sn3.9Ag0.6Cu Solder Alloy, Journal of Electronic Packaging, V. 126(2), pp. 208–212, 2004.
43. J. H. L. Pang, B. S. Xiong, T. H. Low, Low Cycle Fatigue Models for Lead-Free Solders, Thin Solid Films V. 462-463, pp. 408–412, 2004.
44. R. Darveaux, Shear Deformation of Lead Free Solder Joints, Proceedings of the 55th Electronic Components and Technology Conference, pp. 882–893, 2005.
45. B. T. Lampe, Room Temperature Aging Properties of Some Solder Alloys, Welding Journal, V. 55(10), pp. 330s–340s, 1976.
46. Y. Miyazawa, T. Ariga Influences of Aging Treatment on Microstructure and Hardness of Sn-(Ag, Bi, Zn) Eutectic Solder Alloys, Materials Transactions of the Japan Institute of Metals, V. 42(5), pp. 776–782, 2001.
47. M. Li, K. Y. Lee, D. R. Olsen, W. T. Chen, B. T. C. Tan, S. Mhaisalkar, Microstructure, Joint Strength and Failure Mechanisms of SnPb and Pb-Free Solders in BGA Packages, IEEE Transactions on Electronics Packaging, V. 25(3), pp. 185–192, 2002.
48. Y. Ding, C. Wang, M. Li, H. S. Bang, Aging Effects on Fracture Behavior of 63Sn37Pb Eutectic Solder During Tensile Tests Under the SEM, Materials Science and Engineering, V. A384, pp. 314–323, 2004.
49. H. Ma, J. C. Suhling, A review of mechanical properties of lead-free solders for electronic packaging, Journal of Material Science, vol44, 1141–1158, 2009
50. H. Ma, Constitutive models of creep for lead-free solders, Journal of Material Science, V.44, 3841–3851, 2009
51. K. E. Yazzie, J. J. Williams, N. C. Phillips, F. De Carlo, and N. Chawla, Multiscale microstructural characterization of Sn-rich alloys by three dimensional (3D) X-ray synchrotron tomography and focused ion beam (FIB) tomography, Materials Characterization, V.70, 33–41, 2012
52. H. Ma, J. C. Suhling, P. Lall, M. J. Bozack, The Influence of Elevated Temperature Aging on Reliability of Lead Free Solder Joints, The proceeding of the 57th electronic components and technology conference (ECTC), pp 653–668, 2007.

53. J. Glazer, Metallurgy of Low Temperature Pb-free Solders for Electronic Assembly, Int. Mater. Rev., 40, No. 2, 65–93 (1995)
54. H. K. Kim and K.N. Tu, Kinetic analysis of the soldering reaction between eutectic SnPb alloy and Cu accompanied by ripening, Physical Reivew B, V. 53, pp. 16027–16034, 1996.
55. J. J. Glazer, Microstructure and mechanical properties of lead free alloys for low cost electronic assembly—A review. Journal of Electronic Material, V. 23(8), pp.693–700, 1994.
56. H. G. Song, J. W. Morris Jr., F. Hua, The Creep Properties of Lead-Free Solder Joints, JOM, V.56, pp. 30-32, 2002.
57. K. W. Moon, W.J. Boettinger, U.R. Kattner, F.S. Biancaniello, and C.A. Handwerker, Experimental and Thermodynamic Assessment of Sn-Ag-Cu Solder Alloys, Journal of Electronic Materials, V. 29, pp.1122–1236, 2000.
58. D.R. Frear, P.T. Vianco, Intermetallic Growth Behavior of Low and High Melting Temperature Solder Alloys, Metall. Trans., V.25A, pp. 1509–1523, 1994.
59. W.K. Choi and H.M. Lee, Effect of soldering and aging time on interfacial microstructure and growth of intermetallic compounds between Sn-3.5Ag solder alloy and Cu substrate, Journal of Electronic Materials, V. 29(10), pp.1207–1213, 2000.
60. A.J. Sunwoo, J.W. Morris Jr., and G.K. Lucey Jr., The growth of Cu-Sn intermetallics at a pretinned copper-solder interface, Metall.Trans. V. A 23A, pp.13231332, 1992.
61. Z. Mei and J.W. Morris, Characterization of eutectic Sn-Bi solder joints, Journal of Electronic Materials, V. 21 (6), pp.599–607, 1992.
62. F. Bartels, J.W. Morris Jr., G. Dalke, W. Gust, Intermetallic phase formation in thin solid-liquid diffusion couples, Journal of Electronic Materials, V.23 (8), pp.787–790, 1994.
63. J.W. Jang, P. G. Kim, K. N. Tu, D. R. Frear, P. Thompson, Solder reaction-assisted crystallization of electroless Ni—P under bump metallization in low cost flip chip technology, Journal of Applied Physics, V.85, pp.8456–8463, 1999.
64. Kumar A, Chen Z, Mhaisalkar SG, Wong CC, Teo PS, Kripesh V. Effect of Ni–P thickness on solid-state interfacial reactions between Sn–3.5Ag solder and electroless Ni–P metallization on Cu substrate, Thin Solid Films, V. 504(1-2), 410–415, 2005.
65. P, Snugosky, P. Arrowsmith, M. Romansky, Electroless Ni/Immersion Au interconnects: Investigation of black pad in wire bonds and solder joints, Journal of Electronic Materials, V.30 (9), 1262–1270, 2001.
66. S. P. Peng, W. H. Wu, C. E. Ho, Y.M. Huang, Comparative study between Sn37Pb and Sn3Ag0.5Cu soldering with Au/Pd/Ni(P) tri-layer structure, Journal of Alloys and Compounds, V.493, pp.431–437, 2010.
67. Y.-C. Lin, T.-Y. Shih, S.-K. Tien, J.-G. Du, Suppressing Ni–Sn–P growth in SnAgCu/Ni–P solder joints, Scripta Materialia, V.56 (1), pp.49–52, 2007.
68. Y. C. Lin, K. J. Wang, J. G. Duh. Detailed Phase Evolution of a Phosphorous-Rich Layer and Formation of the Ni-Sn-P Compound in Sn-Ag-Cu/Electroplated Ni-P Solder Joints, Journal of Electronic Materials, V.39 (3):283–294, 2010
69. K.N. Tu, K. Zeng,Tin–lead (SnPb) solder reaction in flip chip technology, Mateirals Science and Engineering R, V.34 (1), pp.1–58, 2001.
70. C. S. Huang, G. Y. Jang, J. G. Duh, Soldering-induced Cu diffusion and intermetallic compound formation between Ni/Cu under bump metallization and SnPb flip-chip solder bumps, Journal of Electronic Materials, V. 33(4), pp.283–289, 2004.
71. S.J. Wang, C.Y. Liu, Retarding growth of Ni3P crystalline layer in Ni(P) substrate by reacting with Cu-bearing Sn(Cu) solders, Scripta Materialia, V.49:813–818, 2003.
72. C. Coston, and N.H. Nachtrieb, Self-Diffusion in Tin at High Pressure, J. Phys. Chem., vol 68(8), p.2219, 1964.
73. B. Dyson, Diffusion of Gold and Silver In Tin Single Crystals, J. Appl. Phys., vol. 37, p.2375, 1966.
74. B. Dyson, Interstitial Diffusion of Copper in Tin, J. Appl. Phys., vol. 38, p.3408, 1967.
75. D.C. Yeh, H.B Huntington, Extreme Fast-Diffusion System - Nickel in Single-Crystal Tin, Phys, Rev. Letters, vol. 53(15), pp.1469–72, 1984.
76. S.K. Case, and J.E. Gueths, Anisotropy of the Temperature -Dependent Resistivity of Tin between 8 and 300 K, Physical Rev. B, vol. 2(10), pp.3843–48, 1970.